Journal of the Optical Society of America A
OPTICS, IMAGE SCIENCE, AND VISION

# Capturing multiple full-scene images with a single camera via aperture stop exploitation

Aaron J. Pung

*Space Dynamics Laboratory, 2340 Alamo Ave, S.E., Albuquerque, New Mexico 87106, USA (aaron.pung@sdl.usu.edu)*

*Received 27 May 2022; accepted 29 June 2022; posted 5 July 2022; published 22 July 2022*

**In an effort to increase the capability of modern camera systems, recent advances in imaging technology have seen the maturation of postprocessing and demosaicing algorithms, multispectral imagers, and scene-splitting techniques. Although highly enabling, each of these methods faces an inherent limitation imposed by the camera's geometry. By reevaluating the fundamental components of the camera, this study presents a new method and paradigm in capturing and processing scene information. The proposed camera design is validated and optimized using Zemax simulations. The results show that light entering a camera can be split into three independent, spatially separated, full-scene images, wherein each image retains all spectral, polarimetric, and relative intensity information of the original scene.** 

https://doi.org/10.1364/JOSAA.465335

## 1. INTRODUCTION

Conventional digital cameras utilize an optical lens column to capture, transport, and focus light from a scene onto photosensitive charge-coupled device (CCD) or complementary metal oxide semiconductor (CMOS) sensors. In color detectors, the pixels are often arranged in a three-color Bayer pattern; light absorbed by the red, green, and blue (RGB) pixels undergoes a process to demosaic the color channels and produce a single image. In turn, objects and materials within each image can be identified and separated during postprocessing with spectral indexing and edge-finding techniques [1,2].

To complement developments in postprocessing, recent research efforts have focused on enhancing the capabilities of the imaging system. Adding a linear polarizer in front of the lens column, for example, improves image contrast by reducing glare and reflections from nonmetallic surfaces. Furthermore, images taken with the polarization filter rotated to 0°, 45°, 90°, and 135° allow the first three Stokes parameters ($S_0$, $S_1$, and $S_2$) to be calculated. In turn, the degree of linear polarization and angle of linear polarization can be derived to provide detailed measurements of surface characteristics, albedo, and illumination within a scene [3,4].

Moreover, the four linear polarizer orientations can be combined into a single polarization filter array and placed within the optical system as a divided aperture [5,6] or divided focal plane [7]. Furthermore, each polarization filter can be combined with a unique spectral filter. Although great care must be taken to properly calibrate the camera system and properly demosaic the resulting data, both the results and their redundancies can be exploited to fully characterize the scene [8–12].

The disadvantage of these approaches lies in the component's position, since any filter placed along the optical axis imposes its functionality on the resulting image. To alleviate this issue, alternative methods have been developed to generate multiple images from the single input scene. Much like multispectral snapshot cameras, images split using prisms [13,14], X-cubes [15], compound optics [16,17], and beam splitters [18,19] can be recombined and analyzed during postprocessing.

Upon closer observation, each of these solutions is found to be lacking. In the case of color polarization filter arrays, spectral and polarimetric data can be extracted during postprocessing, but the camera only collects one image. In cases where an additional unfiltered baseline image is desired or overall data collection would benefit from capturing data sets separately, capturing a single image within the camera system is not optimal. In systems that spectrally or polarimetrically split the incident scene, none of the resulting images independently contain all spectral, polarimetric, and relative intensity data from the scene. Last, the pyramid prism array imaging system manages to generate multiple images in a way that preserves spectral information; however, the reduced size of the resulting images ultimately limits the camera's resolution.

This study presents an alternative approach to overcome the limitations in each of the previous systems. The proposed aperture stop exploitation camera (ASTEC) system places a reflective component along the optical axis to exploit properties of the aperture stop. Based on the location and geometry of the new component, incoming light rays are split into three independent spatially separated images, in which each image retains all spectral, polarimetric, and relative intensity information of the original scene.

## 2. APERTURE STOP

From digital single-lens reflex (DSLR) to smartphone cameras, the size and configuration of a camera's lens system varies greatly based on its application and allowable footprint. Despite their differences, however, many camera systems share fundamental similarities in their design. For instance, while the layout of a simple imaging system (Fig. 1) significantly differs from those of other modern lens systems, e.g., DSLR retrofocus lenses or modern aspherical mirror-less camera lenses [20], each shares a "front" set of lenses, an aperture stop, a "rear" set of lenses, and an image sensor.

The location of the aperture stop is significant for two reasons. First, the plane of the aperture stop is the only location along the optical axis where each ray bundle from the scene lies concentrically along the optical axis. Second, in some optical systems, it is the narrowest point within the optical system containing all ray bundles to be imaged on the sensor, making it an ideal location to place a spatially compact division-of-aperture filter [10]. Although not always the case, light rays passing through the aperture stop in some imaging systems have already begun to converge; this is true for geometries like the classical mirrorless-camera lens and Petzval field flattener but not for wide-angle inverted telephoto lenses. While the resulting images may not be ideal, this means that light passing through the aperture stop would still form an image on a detector even if the rear set of lenses was not present.

## 3. REFLECTIVE COMPONENT DESIGN

### A. Geometry

To exploit the features of the aperture stop, a light redistribution optic (LRO) was designed to split the incident light into two reflected images and one transmitted image such that each image contains the full view of the scene and all spectral and polarimetric information is retained. For simplicity, the initial LRO geometry was designed to be used with a basic imaging system in which light rays converge as they pass through the aperture stop. The optical system used in this study is the double gauss experimental arrangement illustrated in Fig. 1.

The geometry of the LRO takes the form of a thin V-shaped reflective component whose apex points in the $-Z$ direction and has elongated edges aligned parallel to the $X$ axis. The top and bottom surfaces of the LRO form a right angle, and each surface sits at a 45° angle to the optical axis. The substrate of the LRO consists of Schott FK3 glass, and the forward-facing ($-Z$) surfaces support a broadband nonpolarizing 50% reflective coating (or $R_c = 0.5$). To minimize internal reflections, the back side of the optic is coated with a broadband antireflection coating. Similarly, unwanted refraction within the LRO is minimized by making the LRO as thin as possible; in these simulations, the distance between the front and rear LRO surfaces is ∼0.2 mm. The LRO is placed near the plane of the aperture stop, ensuring that its width and height need not exceed the diameter of the largest lens in the array.

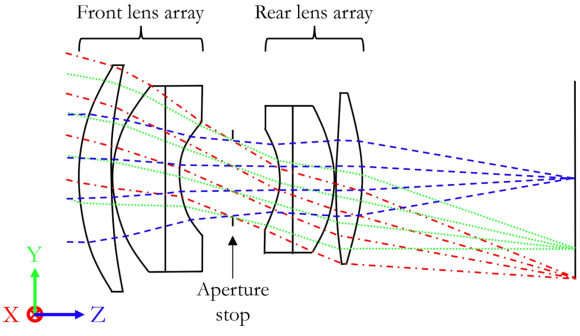


**Fig. 1.** Ray trace through the double gauss experimental arrangement example in Zemax. Changes in ray pattern and color indicate different field positions.

In this configuration, the LRO splits the incident light into three independent and spatially separated images. The top ($+Y$) and bottom ($-Y$) LRO surfaces reflect light from the incident scene toward the top and bottom of the camera housing, respectively, while the transmitted image continues along the optical axis ($+Z$) toward the original sensor. Furthermore, the convergence of the light rays prior to reaching the aperture stop suggests the rear lens array can be removed entirely as shown in Fig. 2. Left untouched, the front lens array continues to produce highly detailed images, but the images are riddled with distortion, astigmatism, and field curvature. As discussed later, these aberrations can be corrected by optimizing parameters of the remaining lens column.

Due to the $R_c = 0.5$ coating on the forward LRO surfaces and the field division at the aperture stop, each top and bottom sensor receives one half of the total reflected light ($0.5 \cdot 0.5 = 0.25$) or 25% of the total incident light. Similarly, the transmitted image carries $1 - R_c$ or 50% of the total incident light to the back-side image sensor. By the same logic, if the reflective LRO coatings were made to have a broadband reflectance of $R_c = 0.66$, each top and bottom sensor would receive roughly 33% of the total incident light, as would the transmitted image. In this case, the intensity is divided equally amongst the three sensors.

The design of the LRO is simple, intuitive, modular, and lightweight. However, the success of its implementation relies heavily on the geometry of its surfaces. The 45° angle of the LRO surfaces is chosen intentionally to redirect the incident rays in a direction generally orthogonal to the optical axis. If the slope angle is changed significantly, the focal plane of the reflected rays becomes stretched along the $Z$ axis, resulting in blurry and elongated images. Furthermore, the resulting images are laterally shifted along the $Z$ axis due to the new angle of incidence between the rays exiting the front lens array and the LRO surfaces. Similarly, the choice of planar LRO faces is intentional since it allows the incoming light rays to continue

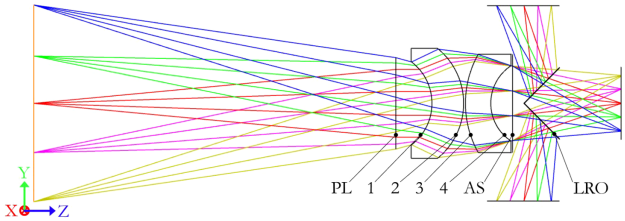


**Fig. 2.** Simulated ray trace through the proposed geometry. Numbered surfaces correspond to surfaces in the Zemax simulation (Table 1). "PL," "AS," and "LRO" represent the paraxial lens, aperture stop, and light redistribution optic, respectively. Different colors represent field position.

their vertical and horizontal convergence. Reflections from nonplanar surfaces, on the other hand, would exacerbate the image's astigmatism or cause some rays to not converge at all, resulting in severe reduction in image quality.

### B. Coatings

The reflected and transmitted images are heavily influenced by the optical coatings applied to the LRO; applying the same coating to both reflective surfaces ensures the top and bottom halves of the transmitted image are identically filtered, but applying different coatings to the reflective surfaces greatly increases the filtering capabilities of the camera. For instance, applying a broadband nonpolarizing 50% reflection coating to each forward-facing surface of the LRO results in three independent spatially separated images, each of which contains the full scene with all spectral, polarimetric, and relative-intensity information. In this case, the process of collecting and analyzing the incoming light is divided across three sensors instead of one, and each image can be independently and uniquely filtered using custom sensor arrays, clip filters, postprocessing algorithms, or some combination thereof.

Alternatively, coating the forward LRO surfaces with different, more exotic thin films allows the ASTEC system to leverage cutting-edge research in thin film design and fabrication technology [21–23]. For instance, a system utilizing calcium fluoride lenses would benefit from >90% transmission between 0.2 and 8.0 μm, covering portions of the ultraviolet (UV), visible (VIS), and infrared (IR) regimes. Coating the top LRO surface with a UV-reflective film would generate a UV image on the top ($+Y$) detector, while coating the bottom LRO surface with an IR-reflective film would generate an infrared image on the bottom ($-Y$) detector. Two such coatings are the "THORK08" and "IR_BLOCK_45L" coatings found in the Zemax coatings database; their spectral reflectance is plotted in Fig. 3. To capture the UV and IR images, commercially available sensors like the Sony IMX487 (UV) or the Thorlabs CS135MUN NIR-Enhanced CMOS (IR) could be used. The final detector is then left to collect light from the transmitted image in the VIS regime; in this case, however, no special detector is needed since the conventional Bayer filter used in many CCD and CMOS VIS cameras collects very little light outside of the 400–700 nm band.

As with any thin film application, attention must be paid to the film's tolerance to changes in wavelength and angle of incidence. As illustrated in Fig. 2, rays exiting the front lens array strike the LRO at a variety of incidence angles. Therefore, the coating applied to the surfaces of the LRO must be tolerant to wavelength as well as variations in incidence angle. Since many thin film designs are geared toward beam-splitting applications, solutions satisfying these criteria are well known in the literature and are commercially available. As one example, the BSW16 50:50 plate beam splitter from Thorlabs provides 50% transmission at an angle of incidence (AoI) of 45° across the visible regime and varies less than 10% for AoI values 30° from the surface normal. Despite their robustness, however, commercially available coatings continue to demonstrate some degree of polarization dependence due to inherent material properties and the difference in optical thickness of each coating layer as seen by the different polarization states at non-normal AoI.

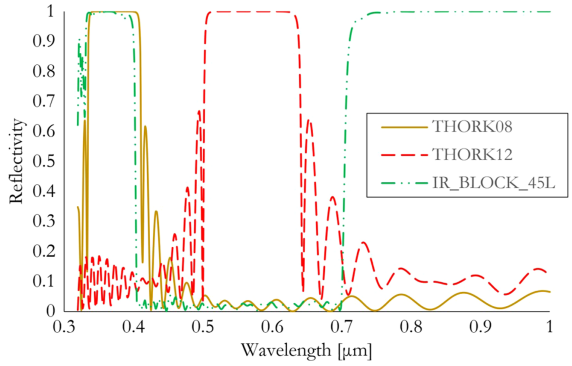


**Fig. 3.** Spectral reflectance for the "THORK08," "THORK12," and "IR_BLOCK_45L" coatings in Zemax.

## 4. SIMULATION AND RESULTS

Numerical validation of the ASTEC system was performed with Zemax OpticStudio. As illustrated in Fig. 2, the simulated ray trace validates the unique features of the aperture stop. By placing the LRO at this location along the optical axis, the LRO only relies on a simple reflective coating to produce three spatially independent images without the need for refraction or polarization-splitting techniques currently seen in the literature.

Removing the rear lens array significantly decreases the weight and size of the camera system, but it also degrades the quality of each image. To compensate, the geometry of the front lens system was optimized to reduce the spot size on the back-side detector using the "Hammer Current" optimization routine. Since no significant field distortions are introduced by the LRO surfaces, the optimization was considered valid for the reflected images as well. Within the optimization, only the surface radii and lens materials were varied. The resulting reflected and transmitted images are illustrated in Fig. 4, and the lens parameters are listed in Table 1. Lens units are in millimeters; the source is unpolarized and defined at blue, green, and red wavelengths (0.460, 0.588, and 0.656 μm, respectively). The "thickness" parameter of each surface specifies the distance between the current surface and the following surface. Using these parameters, the resulting merit function value is 0.034.


**Fig. 4.** (a) Input image is shown alongside simulated images from the (b) top, (c) bottom, and (d) back-side sensor.

**Table 1. Optimized Parameters of the Front Lens Array[a]**

| Surface | Radius [mm] | Thickness [mm] | Material |
|---|---|---|---|
| PL | – | 10.000 | – |
| 1 | −14.281 | 8.747 | LASF35 |
| 2 | −19.373 | 0.500 | LASF35 |
| 3 | 27.523 | 7.000 | P-SF68 |
| 4 | 12.338 | 6.000 | N-LASF31A |
| AS | Infinity | 3.050 | – |

[a]Surface numbers correspond to those labeled in Fig. 2.

Following the optimization, the reflected and transmitted images were simulated using the Image Simulation application in Zemax. By default, this routine convolves the source bitmap image with an array of point spread functions to simulate the formation of an image. Using this method, the geometry of the LRO is problematic because its apex is defined by a single edge stretched between two nodes along the $X$ axis. When the on-axis chief ray of the simulation encounters the leading edge of the LRO, the chief ray is not able to be traced to the top or bottom detector and the simulation fails to produce an image. To circumvent this issue, the LRO can be moved slightly (∼0.1 mm) along the $Y$ axis, displacing the singularity from the optical path of the chief ray. In this case, simulated images are produced, but the layout is inaccurate due to the off-axis nature of the LRO.

Instead, Zemax's geometric bitmap image analysis (GBIA) was used to simulate images on each detector, enabling the LRO to be correctly placed along the optical axis. Compared with the previous method, GBIA uses the bitmap image file as the source, relying on geometrical ray tracing data to produce a simulated image. Within the GBIA routine, rays created by each pixel of the bitmap image are randomly chosen from locations within the source pixel. Similarly, coordinates for the entrance pupil location are also randomly chosen for each ray. Once created, each ray is traced through the optical system; unless the ray is vignetted or encounters an error, the detector collects the intensity of the ray in the appropriate color channel and uses it to produce the simulated RGB image.

While the GBIA routine is highly enabling, interpretation of its results must be done with caution. For instance, the randomized nature (and finite number) of optical rays traced though the imaging system results in images that incorrectly appear to suffer from a loss of detail and an abundance of noise. Additionally, the RGB images generated by GBIA are based on the normalized counts in each detector pixel. This means that, when the relative brightness of the transmitted and reflected images are compared, they will not show the difference in overall image brightness previously discussed.

The simulated images for the top ($+Y$), bottom ($-Y$), and back-side detector are illustrated in Figs. 4(b)–4(d), respectively. In each image, the detector is defined as an 8800 × 7200 array of pixels, each pixel has 1.75 μm on a side and 1000 rays are traced to each pixel. The proposed camera system is illustrated in Fig. 5, scaled to the dimensions of the ray trace.

Subsequent aberration analysis was performed to determine the largest sources of errors within the current ASTEC configuration. Due to model inconsistencies caused by the interaction of the chief ray with the apex of the LRO, however, aberration analysis can only be done on the back-side image.

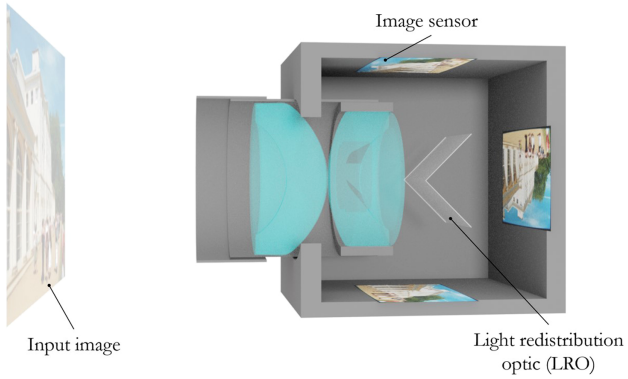


**Fig. 5.** Scaled illustration of the proposed camera system.

Although optimization could be performed by approximating the LRO with a planar (non-V-shaped) mirror tilted at 45°, it is assumed that the optimization of the transmitted image is also valid for the top and bottom reflected images since there are no significant field distortions caused by the surfaces of the LRO. While all seven aberration types (spherical aberration, coma, astigmatism, field curvature, distortion, axial color, and lateral color) are present at each lens surface, the summation of all the aberrations seen in the resulting images is dominated by spherical aberration. By comparison, the magnitude of the spherical aberration (0.302 mm) is roughly three times the magnitude of the second-largest aberration–distortion (−0.105 mm) at 588 nm wavelength; the third-largest aberration is astigmatism (0.048 mm).

## 5. DISCUSSION

The proposed method provides a novel and intuitive way to simultaneously increase a camera system's capabilities while decreasing its size and weight. However, implementing this solution is not without cost since significant changes to the hardware and software infrastructure will likely drive an increase in overall price.

In addition to the cost of two new sensors and their physical mounts inside the ASTEC housing, each sensor will require power from the electrical system, storage space in on-board memory, and processing resources to demosaic images in real time. Similarly, components will require time and resources to fabricate, including the custom lenses, a mechanical holder to support the lenses, and a lens mount to attach the lens system to the camera body. Much like the lenses, the LRO will also require fabrication, thin film coating, and mounting hardware to support its position within ASTEC.

Furthermore, if the LRO mounting hardware is designed to be removable; thus, the LRO can be swapped out quickly during experiments, further increasing the camera's flexibility. On the one hand, this is an enormous benefit, i.e., exchanging the LRO in an ASTEC system during an experiment enables the camera to quickly capture three images for each unique LRO component. On the other hand, each sensor needs to be able to independently change its ISO rating and integration time to accommodate for large variations in scene brightness. The third sensor variable, aperture setting, is shared across all three sensors

due to the relative position of the LRO with respect to the aperture stop. Finally, light collected by the calibrated sensors would require preprocessing to convert the discrete pixel values into images and subsequently store them in a useful format such as PNG or JPEG [24–26].

With all this in mind, the threefold increase in sensor surface area makes the ASTEC well suited for a wide variety of applications, particularly when the forward LRO surfaces are coated with minimally polarizing 50% reflectivity coatings. Two such examples are briefly discussed below.

The first situation concerns highly complex and energetic events such as detonations. In this case, the ASTEC system is able to fully and simultaneously characterize the spectral signature, structure, and emission of the fireball using commercially available detectors. While the dynamic range could be obtained using a variable neutral density clip filter, high-density spectral information could be recorded using a monochrome hyperspectral detector similar to Canon's XNiteCanon5DMK4-HS DSLR sensor. Meanwhile, spectral emission characteristics need only use an imaging detector specific to the infrared.

As a second application, the ASTEC system is capable of removing limitations faced by other sophisticated imaging systems. In situations where color polarization filters are used as divided apertures [10], the data collection and postprocessing are inherently limited by the number of spectral bands on the on-chip color filters; for a single three-color detector, the system is limited to capturing nine spectral bands. Alternatively, an ASTEC could utilize three separate image sensors, each with three unique color bands and covered with a custom color-polarization filter. In this configuration, the maximum color band limitation is increased threefold to 27 spectral channels, which is more than adequate for multispectral index analysis of natural and explosive materials [27,28].

## 6. CONCLUSION

This study introduces and explores the concept of a new multisensor imaging system. In this numerically validated approach, properties of the aperture stop are exploited using a V-shaped light redistribution optic. Based on its simple and intuitive geometry, the LRO enables light from a scene to be split into three independent and spatially separated images, each of which contain the full scene and all its spectral, polarimetric, and relative intensity information. Leveraging advances in thin film technology and postprocessing algorithms, each image can be uniquely collected, filtered, and analyzed to provide a customized, in-depth, multifaceted characterization of the scene.

**Acknowledgment.** A. Pung thanks his colleagues at Space Dynamics Laboratory and the Air Force Research Laboratory for their support, expertise, and insightful discussions.

**Disclosures.** The authors declare no conflicts of interest.

**Data availability.** No data were generated or analyzed in the presented research.

## REFERENCES

1. G. Xin, C. Ke, and H. Xiaoguang, "An improved Canny edge detection algorithm for color image," in *IEEE Proceedings 10th International Conference on Industrial Informatics* (2012).
2. K. Wang, H. Chen, L. Cheng, and J. Xiao, "Variational-scale segmentation for multispectral remote-sensing images using spectral indices," Remote Sens. **14**, 326 (2022).
3. M. Kupinski, C. Bradley, D. Diner, F. Xu, and R. Chipman, "Angle of linear polarization images of outdoor scenes," Opt. Eng. **60**, 082419 (2021).
4. S. Qiu, Q. Fu, C. Wang, and W. Heidrich, "Linear polarization demosaicking for monochrome and colour polarization focal plane arrays," Comput. Graph. Forum **40**, 77–89 (2021).
5. J. L. Pezzaniti and D. B. Chenault, "A division of aperture MWIR imaging polarimeter," Proc. SPIE **5888**, 58880V (2005).
6. J. S. Tyo, D. L. Goldstein, D. B. Chenault, and J. A. Shaw, "Review of passive imaging polarimetry for remote sensing applications," Appl. Opt. **45**, 5453–5469 (2006).
7. V. Gruev, "Fabrication of a dual-layer aluminum nanowires polarization filter array," Opt. Express **19**, 24361–24369 (2011).
8. S. Mihoubi, P.-J. Lapray, and L. Bigué, "Survey of demosaicking methods for polarization filter array images," Sensors **18**, 3688 (2018).
9. P.-J. Lapray, "Exploiting redundancy in color-polarization filter array images for dynamic range enhancement," Opt. Lett. **45**, 5530–5533 (2020).
10. S. Ono, "Snapshot multispectral imaging using a pixel-wise polarization color image sensor," Opt. Express **28**, 34536–34573 (2020).
11. Y. Giménez, P.-J. Lapray, A. Foulonneau, and L. Bigué, "Calibration algorithms for polarization filter array camera: Survey and evaluation," J. Electron. Imaging **29**, 041011 (2020).
12. M. Morimatsu, Y. Monno, M. Tanaka, and M. Okutomi, "Monochrome and color polarization demosaicking based on intensity-guided residual interpolation," IEEE Sens. J. **21**, 26985–26996 (2021).
13. V. Akondi, S. Castillo, M. A. Jewel, and B. Vohnsen, "Digital pyramid wavefront sensor," in *Imaging and Applied Optics* (2013).
14. V. Hutterer, R. Ramlau, and I. Shatokhina, "Real-time adaptive optics with pyramid wavefront sensors: Part I. A theoretical analysis of the pyramid sensor model," Inverse Prob. **35**, 045007 (2019).
15. B. Dong, F. Zeng, and B. Pan, "A simple and practical single-camera stereo-digital image correlation using a color camera and X-cube prism," Sensors **19**, 4726 (2019).
16. W.-S. Sun, C.-L. Tien, C.-Y. Chen, and D.-C. Chen, "Single-lens camera based on a pyramid prism array to capture four images," Opt. Rev. **20**, 145–152 (2013).
17. J. Liu, J. Chen, J. Liu, S. Feng, X. Li, and J. Cui, "Optical design of a prism-grating-based lenslet array integral field spectrometer," Opt. Express **26**, 19456–19469 (2018).
18. J. C. Ramella-Roman, K. Lee, S. A. Prahl, and S. L. Jacques, "Design, testing, and clinical studies of a handheld polarized light camera," J. Biomed. Opt. **9**, 1305–1310 (2004).
19. D. Freiman, Z. Elgart, and A. Chernoborov, "Dichroic beamsplitter for a dual-wavelength camera in a long-range airborne reconnaissance system," Proc. SPIE **5783**, 827–834 (2005).
20. V. Blahnik and O. Schindelbeck, "Smartphone imaging technology and its applications," Adv. Opt. Technol. **10**, 145–232 (2021).
21. R. R. Willey, "Designing edge filters, high reflectors, polarizing and non-polarizing beamsplitters," in *Field Guide to Optical Thin Films* (2006).
22. P. Favreau, C. Hernandez, A. S. Lindsey, D. F. Alvarez, T. Rich, P. Prabhat, and S. J. Leavesley, "Thin-film tunable filters for hyperspectral fluorescence microscopy," J. Biomed. Opt. **19**, 011017 (2013).
23. I. J. Hodgkinson, M. W. McCall, and Q. Wu, *Birefringent Thin Films and Polarizing Elements* (Imperial College, 2015).
24. P.-J. Lapray, X. Wang, J.-B. Thomas, and P. Gouton, "Multispectral filter arrays: Recent advances and practical implementation," Sensors **14**, 21626–21659 (2014).
25. L. Yu and B. Pan, "Full-frame, high-speed 3D shape and deformation measurements using stereo-digital image correlation and a single color high-speed camera," Opt. Lasers Eng. **95**, 17–25 (2017).

26. B. Pan, L. Yu, and Q. Zhang, "Review of single-camera stereo-digital image correlation techniques for full-field 3D shape and deformation measurement," Sci. China Technol. Sci. **61**, 2–20 (2017).
27. M. V. A. Murzina and J. P. Farrell, "Dynamic hyperspectral imaging," Proc. SPIE **5769**, 135–144 (2005).
28. S. Morsy, A. Shaker, A. El-Rabbany, and P. E. LaRocque, "Airborne multispectral lidar data for land-cover classification and land/water mapping using different spectral indexes," ISPRS Ann. Photogram. Remote Sens. Spatial Inf. Sci. **III-3**, 217–224 (2016).